The first crystal structure of human RNase 6 reveals a novel substrate-binding and cleavage site arrangement

Guillem Prats-Ejarque*, Javier Arranz-Trullén*, Jose A. Blanco*, David Pulido*[1], M. Victòria Nogués*, Mohammed Moussaoui* and Ester Boix*[2]

*Department of Biochemistry and Molecular Biology, Faculty of Biosciences, Universitat Autònoma de Barcelona, E-08193 Cerdanyola del Vallès, Spain

Human RNase 6 is a cationic secreted protein that belongs to the RNase A superfamily. Its expression is induced in neutrophils and monocytes upon bacterial infection, suggesting a role in host defence. We present here the crystal structure of RNase 6 obtained at 1.72 Å (1 Å = 0.1 nm) resolution, which is the first report for the protein 3D structure and thereby setting the basis for functional studies. The structure shows an overall kidney-shaped globular fold shared with the other known family members. Three sulfate anions bound to RNase 6 were found, interacting with residues at the main active site (His^{15}, His^{122} and Gln^{14}) and cationic surface-exposed residues (His^{36}, His^{39}, Arg^{66} and His^{67}). Kinetic characterization, together with prediction of protein–nucleotide complexes by molecular dynamics, was applied to analyse the RNase 6 substrate nitrogenous base and phosphate selectivity. Our results reveal that, although RNase 6 is a moderate catalyst in comparison with the pancreatic RNase type, its structure includes lineage-specific features that facilitate its activity towards polymeric nucleotide substrates. In particular, enzyme interactions at the substrate 5′ end can provide an endonuclease-type cleavage pattern. Interestingly, the RNase 6 crystal structure revealed a novel secondary active site conformed by the His^{36}–His^{39} dyad that facilitates the polynucleotide substrate catalysis.

Key words: kinetic characterization, molecular dynamics, protein crystallography, RNase A superfamily, RNase k6, sulfate anion.

INTRODUCTION

Human RNase 6 is a protein belonging to the bovine pancreatic ribonuclease A (RNase A) superfamily, a vertebrate-specific family comprising small secretory proteins, sharing a common overall 3D structure and displaying a variety of properties. Together with the first ascribed function of pancreatic RNases to digest RNA, several family members were reported to be involved in innate immunity, showing toxicity towards a wide spectrum of pathogens, from viruses, bacteria, fungi and protozoa to helminth parasites [1–3]. An unusually high evolution rate within the family and the antimicrobial properties of distantly related members suggested a common ancestral innate immunity role [4,5]. In humans, the family includes eight known members, also called the 'canonical RNases' (Figure 1A). Despite their low sequence identity, ranging from 30 % to 70 %, we observe the conservation of the disulfide bonding pattern and the catalytic triad. All members are highly cationic and are localized at the long arm (q) of human chromosome 14 [6,7].

RNase 6, also named RNase k6, was first to be identified during a genomic search for a homologous protein of bovine kidney RNase (RNase k2) and localized on q11 region of chromosome 14 [8,9]. The newly identified human mature protein sequence was found to share 72 % identity with its bovine RNase k2 counterpart. Divergence of the kidney RNases in comparison with the prototype reference family pancreatic type RNases supported their involvement in a differentiated biological role. Due to the presence of human RNase 6 in a large variety of tissues and its expression in monocytes and neutrophils, it was proposed that it could play a role in host defence. Indeed, recent studies by Becknell et al. [10] showed the protein expression in macrophages and epithelial cells at the urinary tract in response to exposure of uropathogenic bacteria. Spencer and co-workers also reported a potent antimicrobial activity *in vitro* against Gram-negative and Gram-positive bacteria for RNase 6, together with its closest homologue, RNase 7, and proposed both proteins as being responsible for the mammalian urinary tract sterility maintenance [11,10]. Experimental evidence was also provided by the reported down-regulation of RNase 6 together with other host innate immunity proteins induced by the human immunodeficiency virus (HIV) [12]. RNase 6 displays 55 % amino acid identity with RNase 7, and belongs to the RNase 6, 7 and 8 cluster, sharing with them common structural features (Figure 1A). Interestingly, even though it has been found that eosinophil RNase 2 and RNase 3 gene lineages have undergone one of the highest rates of divergent evolution to produce paralogous genes [13,14], RNase 6 primate gene lineages appear to have evolved in a more conservative mode [9]. On the other hand, a contradictory scenario has been reported in rodents, in which the evolution of RNase 6 presents a substantially higher rate [15]. All in all, a similar tendency towards an isoelectric point increase is shared within the eosinophil lineage.

The RNase A superfamily members share a conserved catalytic mechanism that was thoroughly characterized thanks to the pioneering enzymology studies during the first half of the XX's century [16–18]. RNase A catalyses the cleavage of the 3′5′ phosphodiester bond of single polynucleotide substrates, showing selectivity for pyrimidines at the main base subsite (B_1) and a preference for purines at the secondary base site (B_2). Degradation of polynucleotide substrate is also assisted by additional binding sites at both sides of the catalytic centre, referred to as B_n, R_n and p_n for bases, ribose and phosphate binding respectively [19].

Preliminary kinetic characterization of RNase 6 upon its discovery indicated a moderate catalytic efficiency with respect

Abbreviations: C>p, cytidine 2′,3′-cyclic phosphate; poly(A), polyadenylic acid; poly(C), polycytidylic acid; poly(U), polyuridylic acid.

[1] Present address: Imperial College London, South Kensington Campus London, London SW7 2AZ, U.K.
[2] To whom correspondence should be addressed (email Ester.Boix@uab.cat).

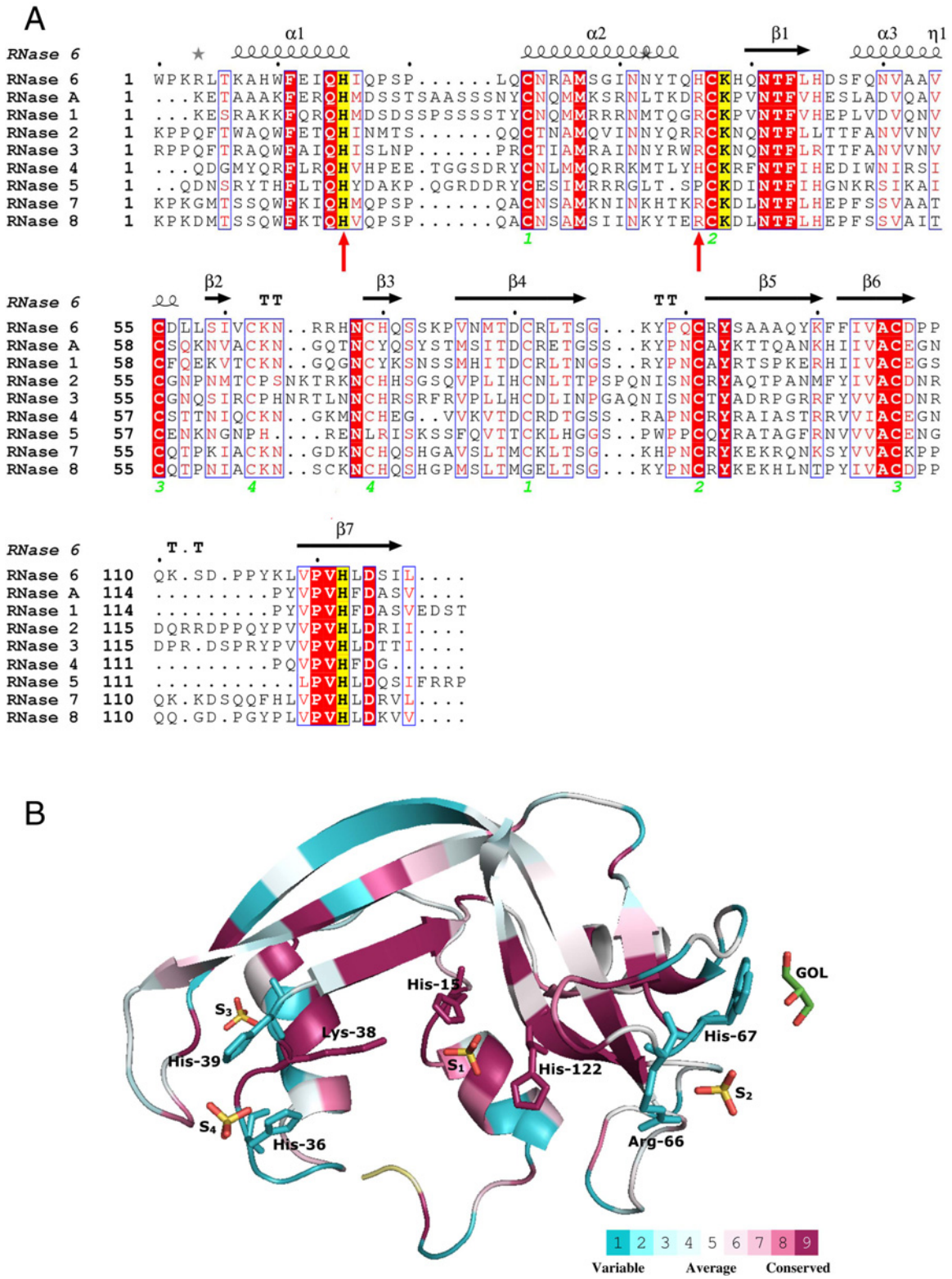

Figure 1 Primary structure of human RNases and 3D structure of RNase 6 coloured by residue conservation score

(**A**) Structure-based sequence of the eight canonical human RNases together with RNase A. The active sites are highlighted in yellow. The four disulfide bonds are labelled with green numbers. Tested mutations on RNase 6 are indicated with red arrows. The alignment was performed using ClustalW, and drawn using ESPript (http://espript.ibcp.fr/ESPript/). Labels are as follows: red box, white character for strict identity; red character for similarity in a group and character with a blue frame for similarity across groups. (**B**) RNase 6 3D structure surface representation using the CONSURF web server (http://consurf.tau.ac.il/) featuring the relationships among the evolutionary conservation of amino acid positions within the RNase A family. The 3D structure shows residues coloured by their conservation score using the colour-coding bar at the bottom. Sulfate anions (S1–S4) and the glycerol (GOL) molecule found in the crystal structure are depicted. Conserved residues belonging to the RNase catalytic site and interacting with bound sulfate anions are labelled.

to the family reference member RNase A. Estimation of kinetic parameters using yeast tRNA as a substrate reported approximately a 40-fold reduced catalytic rate in comparison with RNase 2 [8]. Further side-by-side comparison of RNase 6 catalytic efficiency confirmed an overall moderate relative catalytic efficiency, higher than that of RNase 3 but significantly lower than that of RNase 7 [20–22].

In the present paper, we describe the first crystal structure of RNase 6. The protein structural analysis is complemented by its enzymatic characterization to highlight RNase 6's singularity within the RNase A family context.

MATERIALS AND METHODS

Expression and purification of the recombinant proteins

A plasmid containing the gene of recombinant human RNase 6 was transformed in a prokaryote expression system. The cDNA encoding RNase 6 sequence was a gift from Dr Helene Rosenberg (National Institutes of Health, Bethesda, MD, U.S.A.). Mutant variants were constructed using the Quik Change Site-Directed Mutagenesis kit (Stratagene). All constructs were confirmed by DNA sequencing and the purified protein was analysed by MALDI–TOF-MS and N-terminal sequencing.

The genes were subcloned in plasmid pET11c for prokaryote high yield expression. *Escherichia coli* BL21(DE3) competent cells were transformed with the pET11c/RNase 6 plasmid. The expression protocol was optimized from the previously described procedure [20] to optimize the RNase 6 final recovery yield. For high yield expression, bacteria were grown in Terrific broth (TB), containing 400 μg/ml ampicillin. Recombinant protein was expressed after cell induction with 1 mM IPTG added when the culture showed a D_{600} of 0.6. The cell pellet was collected after 4 h of culture at 37 °C. Cells were resuspended in 10 mM Tris/HCl and 2 mM EDTA, pH 8, and sonicated at 50 W for 10 min with 30-s cycles. After centrifugation at 15 000 ***g*** for 30 min, the pellet fraction containing inclusion bodies was processed as follows: the pellet fraction was washed with 50 mM Tris/HCl, 2 mM EDTA and 0.3 M NaCl, pH 8, and after centrifugation at 20 000 ***g*** for 30 min, the pellet was dissolved in 12 ml of 6 M guanidinium chloride, 0.1 M Tris/acetate and 2 mM EDTA, pH 8.5, containing 80 mM GSH, and incubated under nitrogen for 2 h at room temperature. The protein was then refolded by a rapid 100-fold dilution into 0.1 M Tris/HCl, pH 7.5, containing 0.5 M L-arginine, and GSSG was added to obtain a GSH/GSSG ratio of 4. Dilution in the refolding buffer was adjusted to obtain a final protein concentration of 30–150 μg/ml. The protein was incubated in refolding buffer for 48–72 h at 4 °C. The folded protein was then concentrated, buffer-exchanged against 0.015 M Tris/HCl, pH 7, and purified by cation-exchange chromatography on a Resource S column equilibrated with the same buffer. The protein was eluted with a linear NaCl gradient from 0 to 2 M in 0.015 M Tris/HCl, pH 7, buffer. Further purification was achieved by reverse-phase chromatography on a Vydac C_4 column, using an acetonitrile gradient. The homogeneity of the purified proteins was checked by SDS/15 % PAGE and Coomassie Blue staining and by N-terminal sequencing. RNase 3 and RNase 7 were expressed as previously described [20,24].

Spectrophotometric kinetic analysis

Polycytidylic acid [poly(C)], polyuridylic acid [poly(U)], polyadenylic acid [poly(A)], poly(A): poly(U), CpA, UpA, UpG and cytidine 2′,3′-cyclic phosphate (C>p) (Sigma–Aldrich) were used as substrates, and the kinetic parameters were determined by a spectrophotometric method as described in [20]. RNase A, used as a control protein, was purchased from Sigma. Assays were carried out in 50 mM sodium acetate and 1 mM EDTA, pH 5.5, at 25 °C, using 1-cm pathlength cells. Substrate concentration was determined spectrophotometrically using the following molar absorption coefficients: $\varepsilon_{268} = 8400\ M^{-1}\cdot cm^{-1}$ for C>p; $\varepsilon_{265} = 21\,000\ M^{-1}\cdot cm^{-1}$ for CpA, $\varepsilon_{261} = 23\,500\ M^{-1}\cdot cm^{-1}$ for UpA, $\varepsilon_{261} = 20\,600\ M^{-1}\cdot cm^{-1}$ for UpG, $\varepsilon_{268} = 6200\ M^{-1}\cdot cm^{-1}$ for poly(C), $\varepsilon_{260} = 9430\ M^{-1}\cdot cm^{-1}$ for poly(U) and $\varepsilon_{260} = 4430\ M^{-1}\cdot cm^{-1}$ for poly(A):poly(U) for each nucleotide unit. The activity was measured by following the initial reaction velocities using the difference molar absorption coefficients, in relation to cleaved phosphodiester bonds: $\Delta\varepsilon_{286} = 1450\ M^{-1}\cdot cm^{-1}$ for CpA, $\Delta\varepsilon_{286} = 570\ M^{-1}\cdot cm^{-1}$ for UpA, $\Delta\varepsilon_{280} = 480\ M^{-1}\cdot cm^{-1}$ for UpG, $\Delta\varepsilon_{250} = 2380\ M^{-1}\cdot cm^{-1}$ for poly(C), $\Delta\varepsilon_{282} = 829\ M^{-1}\cdot cm^{-1}$ for poly(U) and $\Delta\varepsilon_{260} = 3400\ M^{-1}\cdot cm^{-1}$ for poly(A):poly(U) for transphosphorylation reaction, and $\Delta\varepsilon_{286} = 1450\ M^{-1}\ cm^{-1}$ for C>p hydrolysis reaction [20,25]. Duplicates of seven substrate concentrations (ranging from 0.1 to 2 mM) were tested for each condition. Final enzyme concentrations were selected from 0.1 to 10 μM depending on the RNase activity for each assayed substrate. Kinetic parameters were obtained by the non-linear regression GraFit data analysis program (Erithacus Software). Relative activity of RNase mutants was calculated by comparison of initial velocities (V_0), using a substrate concentration of 0.1 mM for dinucleotides and 0.5 mg/ml for polynucleotides.

Activity staining gel

Zymograms were performed following the method previously described [26]. SDS/15 % polyacrylamide gels were cast with 0.3 mg/ml poly(C) (Sigma–Aldrich) and run at a constant current of 40 mA for 1.5 h. Then, the SDS was extracted from the gel with 10 mM Tris/HCl, pH 8, and 10 % (v/v) propan-2-ol. The gel was then incubated in the activity buffer (0.1 M Tris/HCl, pH 8) to allow enzymatic digestion of the embedded substrate and then stained with 0.2 % (w/v) Toluidine Blue (Merck) in 10 mM Tris/HCl, pH 8, for 10 min. Positive bands appeared white against the blue background. The loading buffer had no 2-mercaptoethanol to facilitate recovery of active enzymes. RNase A (Sigma–Aldrich) was used as a control.

Analysis of polynucleotide cleavage pattern

The characterization of the RNases, substrate cleavage patterns was carried out by studying the digestion product profiles, as previously described [27]. The poly(C) substrate (Sigma–Aldrich) was dissolved at a concentration of 0.5 mg/ml in 10 mM HEPES/KOH at pH 7.5. Then, 50 μl of the poly(C) solution was digested with 10 μl of enzyme solution at 25 °C for 1 h. Enzyme final concentrations were adjusted for each RNase: 50 nM for RNase 6 and RNase 6-H36R and 1.4 μM for RNase 6-H15A and RNase 7-H15A. At different digestion times the products of the reaction were separated by reverse-phase HPLC (Nova Pak C_{18}, Waters) according to the previously described procedure [27,28]. Briefly, the RNase/poly(C) reaction mixtures (50 μl and 15 μl for wild-type and mutant RNase 6 respectively) were injected on to the column equilibrated with solvent A (10 % (w/v) ammonium acetate and 1 % (v/v) acetonitrile) and the elution was carried out by an initial 10-min wash and 50-min gradient from 100 % solvent A to 10 % solvent A plus 90 % solvent B (10 % (w/v) ammonium acetate and 11 % (v/v) acetonitrile). Product elution was detected from the absorbance at 260 nm,

and peak identification was performed according to previous characterization of oligocytidylic acids [29].

Protein crystallization

RNase 6 crystals were obtained after high-throughput screening of available commercial kits by the hanging-drop vapour-diffusion methodology at 20 °C. In one of these kits, JCSG-plus™ HT-96 (Molecular Dimensions), RNase 6 at 10 mg/ml was able to crystallize under one condition (0.2 M NaCl, 0.1 M sodium cacodylate, and 2 M $(NH_4)_2SO_4$, pH 6.5). This condition was optimized to improve the crystal size by the hanging-drop methodology by mixing 1 μl of the protein sample with 1 μl of the crystallization buffer. The best condition resulting from this optimization was 0.05 M NaCl, 0.1 M sodium cacodylate (pH 6.5) and 2 M $(NH_4)_2SO_4$. Cubic crystals appeared after 10 days of incubation at 20 °C and were soaked in the cryoprotectant solution by adding 15 % glycerol to the crystallization buffer prior to X-ray exposure.

Data collection, processing and protein structure solving

Data were collected at the XALOC BL13 beamline station of ALBA synchrotron (Spain) using a wavelength of 0.9795 Å. Data collection was performed at 100 K using a Pilatus 6M detector (Dectris®), 800 images were taken at $t_{exp} = 0.2$ s, $\Delta\varphi = 0.2°$. The data obtained were processed with XDS (MPI for Medical Research) [30]. The structure was solved by molecular replacement with Phenix Phaser-MR program using an RNase 6 model constructed upon NMR structure of RNase 7 (PDB ID: 2HKY) [31]. Iterative cycles of refinement and manual building were applied using PHENIX [32] and Coot [33] respectively until no further improvement of R_{free} could be achieved. Finally, the stereochemistry of the structure was validated with SFCHECK [34] and WHAT_CHECK [35]. Table 1 shows the data collection and structure refinement statistics.

Table 1 Data collection, processing and structure refinement parameters for the RNase 6 crystal structure (PDB ID: 4X09)

*$R_{merge} = \Sigma_{hkl}\ \Sigma_{j\text{-}1}$ to $N|I_{hkl}\text{-}I_{hkl}(j)|/\ \Sigma_{hkl}\ \Sigma_{j\text{-}1}$ to $N\ I_{hkl}(j)$, where N is the redundancy of the data. †Outermost shell is 1.78–1.72 Å. ‡$R_{crystal} = \Sigma_h|F_o\text{-}F_c|/\Sigma_h F_o$, where F_o and F_c are the observed and calculated structure factor amplitudes of reflection h respectively. §R_{free} is equal to R_{cryst} for a randomly selected 5 % subset of reflections not used in the refinement.

Parameter	Value
Data collection	
Space group	$P2_12_12_1$
Unit cell	
a, b, c (Å)	27.73, 38.86, 97.97
α, β, γ (°)	90.0, 90.0, 90.0
Number of molecules in asymmetric unit	1
Resolution (Å)	1.72
Number of total reflections	22981
Number of unique reflections	11717
R_{merge}*,† (%)	2.8 (23.4)
$I/\sigma I$†	13.0 (2.4)
Completeness for range† (%)	99.2 (99.0)
Wilson B factor (Å^2)	24.7
Matthews coefficient (Å^3/Da)	1.80
Solvent content (%)	31.71
Refinement	
Resolution range (Å)	48.98–1.72
R_{cryst}‡/R_{free}§ (%)	19.28/22.67
Number of protein atoms	1068
Number of water molecules	124
Number of bound anions	4
RMSD from ideality	
In bond lengths (Å)	0.004
In bond angles (deg)	0.908
Average B factors (Å^2)	
All protein atoms	30.34
Main-chain atoms	27.30
Side-chain atoms	33.23
Sulfate anion atoms	57.60
Glycerol atoms	49.55
Water molecules	40.67

Structure modelling

Molecular modelling predictions were carried out using protein–nucleotide docking and molecular dynamics (MD) simulations. Docking simulations were conducted with AutoDock 4.2.6 (Scripps Research Institute) and MD simulations were performed with GROMACS 4.5.5 [36]. RNase A and RNase 6 complexes with dinucleotides (CpA, UpA and UpG) were predicted. The initial RNase A–dinucleotides' positions were determined on the basis of crystallographic data of RNase A bound to d(CpA) [37]. For RNase 6–dinucleotide complexes, the position of the S1 sulfate was taken as reference. Due to the inactive position of His^{122} in the RNase 6 crystal, the position of the histidine was adjusted to the 'active' conformation taking RNase A as a reference (PDB ID: 1RPG).

For MD simulations the force field AMBER99SB-ILDN [38] was used both for protein and RNA components. All of the complexes were centred in a cubic cell with a minimum distance of box to solute of 1.0 nm. The unit cell was filled with transferable intermolecular potential 3P (TIP3P) water [39] in neutral conditions with 150 mM NaCl. Neighbour search was performed using a group cut-off scheme with a cut-off of 1.4 nm for van der Waals interactions and 0.9 nm for the other short-range Lennard–Jones interactions. For long range interactions, smooth particle mesh of Ewald (PME) [40,41] was used with a fourth-order interpolation scheme and 0.16-nm grid spacing for FFT. The bonds were constrained with the P-LINCS algorithm [42], with an integration time step of 2 fs. The energy of the system was minimized using the steepest descendant algorithm and equilibrated in two steps. First, an initial constant volume equilibration (NVT) of 100 ps was performed with a temperature of 300 K using a modified Berendsen thermostat. Then, 100 ps of constant pressure equilibration (NPT) was run at 1 bar (100 kPa) with a Parrinello–Rahman barostat [43,44] at 300 K and the same thermostat. Finally, 20 ns production runs were performed under an NPT ensemble without applying restraints. Three independent simulations in periodic boundary conditions were conducted for each complex. The evolution of the average RMSD for all non-hydrogen ligand atoms after least-squares fitting to the original position was calculated.

For prediction of the RNase 6–heptanucleotide complex, the RNase A–d(ATAA) crystal structure was taken as a reference (PDB ID: 1RCN [45]). First, the d(ATAA) co-ordinates were used to build an AUAA ribonucleotide. His^{122} of RNase 6 was fixed in the corresponding active conformation. Local search docking with 2000 cycles and 2000 iterations was performed with AutoDock 4.2.6 [46] to adjust the AUAA position to RNase 6 active site. Then, three cytidines were added to the 5′ end of the tetranucleotide. The sulfate positions of the RNase 6 structures were taken as a reference to place the phosphates corresponding to the extended nucleotide. Then, a steepest descent energy minimization of the complex was performed with GROMACS

4.5.5. MD simulations were also applied using the same protocol described for dinucleotides.

Prediction of pK_a values

Prediction of pK_a values of selected protein residues was performed using the Rosetta online server ROSIE [47]. The estimated pK_a values of selected histidine residues were calculated by using a neighbour sphere of 15 Å and considering the protonation state of ionizable residues. A starting pK_a reference value of 6.3 for each histidine residue was ascribed. The program evaluates all potential conformational rotamers together with the influence of side chain and backbone mobility. RNase A (PDB ID: 7RSA) co-ordinates were used as a reference control. Predicted pK_a values for His^{12}, His^{105} and His^{119} in RNase A were found in accordance with the previously reported experimental values [48]. His^{105} in RNase A and His^{67} in RNase 6 were selected as control solvent-exposed residues, not involved in Coulombic interactions with nearby residues. The RNase A double mutant (RNase A-H7H10) [49] crystal structure (PD ID: 5ET4; Blanco, Salazar, Moussaoui and Boix unpublished results) was also analysed to evaluate the predicted pK_a values for an engineered secondary site located at RNase A secondary phosphate-binding site.

RESULTS

RNase 6 3D structure

RNase 6 crystals diffracted to 1.72 Å. The structure was solved using RNase 7 structure as a model (PDB ID: 2HKY [31]). The crystallographic statistics for the data collection, processing and structure solving are provided in Table 1. Structural data for RNase 6 structure are available in the PDB under the accession number 4X09. The RNase 6 3D structure (Figure 1B) complies with the RNase A superfamily overall conformation, with a kidney-shaped structure formed by seven β-strands and three α-helices cross-linked by four conserved disulfide bonds, as listed in Supplementary Table S1. Loop residues Trp^1–Lys^3, Gln^{17}–Leu^{21}, Lys^{63}–Arg^{66}, Gly^{86}–Gln^{90} and Pro^{108}–Ser^{112} are partially disordered. In particular, practically no electron density was visualized for residues Pro^2, Lys^3, Gln^{17}, Leu^{21}, Gly^{86} and Lys^{87} that could not be properly modelled. Alternative side-chain conformations were modelled for some residues (Gln^{14}, Asn^{32}, Ser^{59}, His^{67}, Met^{78} and Thr^{79}). Specifically, high motion values were observed in loops L1, L2 and L8, where 4% of the residues are disordered, as reported for the RNase 7 structure [31]. Residues involved in crystal packing were analysed by the PISA web server [50]. The intermolecular contacts are listed in Supplementary Table S2. Interactions are found mostly between β3, β4, β5 and β7 strand residues (Gln^{71}, Arg^{82}, Ala^{97}–Tyr^{99}, Ser^{125} and Ile^{126}) and loop residues. No packing contacts are seen in the environment of the active site, therefore enabling further substrate-binding studies.

An overall comparison of RNase 6 crystal structure with previously solved structures of RNase A superfamily members highlighted some interesting particularities. First, we observed a distinct conformation of the RNase 6 N-terminus, where Trp^1, unique in the RNase A superfamily, folds back towards the protein core. Next, we found several non-conserved histidine residues, unique to RNase 6, that contribute to the protein structure peculiarities. His^9 was observed to interact with Glu^{12} by a salt bridge, which would participate in the stabilization of the first α-helix, as reported in RNase A for the Glu^2–Arg^{10} salt bridge [51,52]. Unusual rotamer conformations, showing an unambiguous electron density, were observed for two non-conserved histidines: His^{36} and His^{67}.

RNase 6 sulfate-binding sites

The protein was crystallized in the presence of ammonium sulfate and four sulfate anions were identified in the crystal asymmetric unit (Figure 1B and Supplementary Figure S1). Three of these sulfates corresponded to defined cationic regions exposed at the protein surface and correlate to putative RNA phosphate-binding sites, whereas the fourth sulfate is involved in the crystal packing. Sulfate anion interactions with nearby residues are listed in Supplementary Table S3 and illustrated in Figure 2. Sulfate labelled S1 corresponds to the active site of the enzyme, conserved in all canonical RNases. The presence of either a sulfate or phosphate anion at the enzyme active site was already reported for RNase A [53,54] and other family members: RNase 2–EDN (eosinophil-derived neurotoxin) [55], RNase 3–ECP (eosinophil cationic protein) [56] and RNase 5–angiogenin [57]. On the other hand, the second sulfate (S2) found in the RNase 6 structure binds to a distinct region not reported in any other family members (Arg^{66}/His^{67}). Comparative studies of our structure with the RNase A–tetranucleotide analogue [45] suggested that this region may represent a distinct phosphate-interaction subsite located at the 5′ end of the RNA substrate. In addition, a third sulfate anion was visualized in the RNase 6 structure bound to two histidine residues (His^{36} and His^{39}), His^{39} being unique to RNase 6 among all RNase A members. Interestingly, both histidine residues together with a close by lysine residue (Lys^{87}) mimic the disposition of a putative RNase active site (Figure 3), as also identified using the PDBeMotif analysis tool available at the PDBe server (http://www.ebi.ac.uk/pdbe-site/pdbemotif/).

RNase 6 main active site

The RNase 6 crystal structure illustrates the conservation of the active-site architecture within the RNase A family. Residues His^{15}, Lys^{38} and His^{122} (His^{12}, Lys^{41} and His^{119} RNase A counterparts) build the active-site groove, with His^{122} adopting the so-called 'inactive' orientation [58], a conformation reported to be favoured in acidic and high ionic salt solutions [59]. Comparison of atomic crystal structures for RNase A indicated that His^{119} can adopt two conformations: A (active) and B (inactive), where the 'active' ring orientation is required for adenine binding at the secondary base B_2 site [37,60]. On the other hand, the active orientation of the RNase A His^{119} ring was reported to be favoured by the hydrogen bond interaction with the vicinal Asp^{121} residue, whose interaction would account for the correct His^{119} tautomer in catalysis [61]. RNase 6 counterpart (Asp^{124}), located in an equivalent conformation, could also perform an equivalent role. However, the inactive His^{122} conformation is fixed in our RNase 6 structure by a hydrogen bond interaction with Lys^7. Therefore, the close proximity of Lys^7 might alter significantly the properties of the His^{122} catalytic residue. Likewise, we considered the potential influence of the nearby His^{36}/His^{39} RNase 6 residues on the other active-site histidine residue (His^{15}). The presence of cationic residues near to the RNase 6 active site could shape the enzyme's performance, and may account for a reduction in its catalytic efficiency in comparison with RNase A (Table 2 and Supplementary Table S4). Although the RNase 6 structure conserves equivalent positions for some key residues at the active-site environment, such as Gln^{14} and Asn^{41} (Gln^{11} and Asn^{44} respectively in RNase A), the close proximity of residues such as Lys^7, His^{36} or His^{39} should not be disregarded.

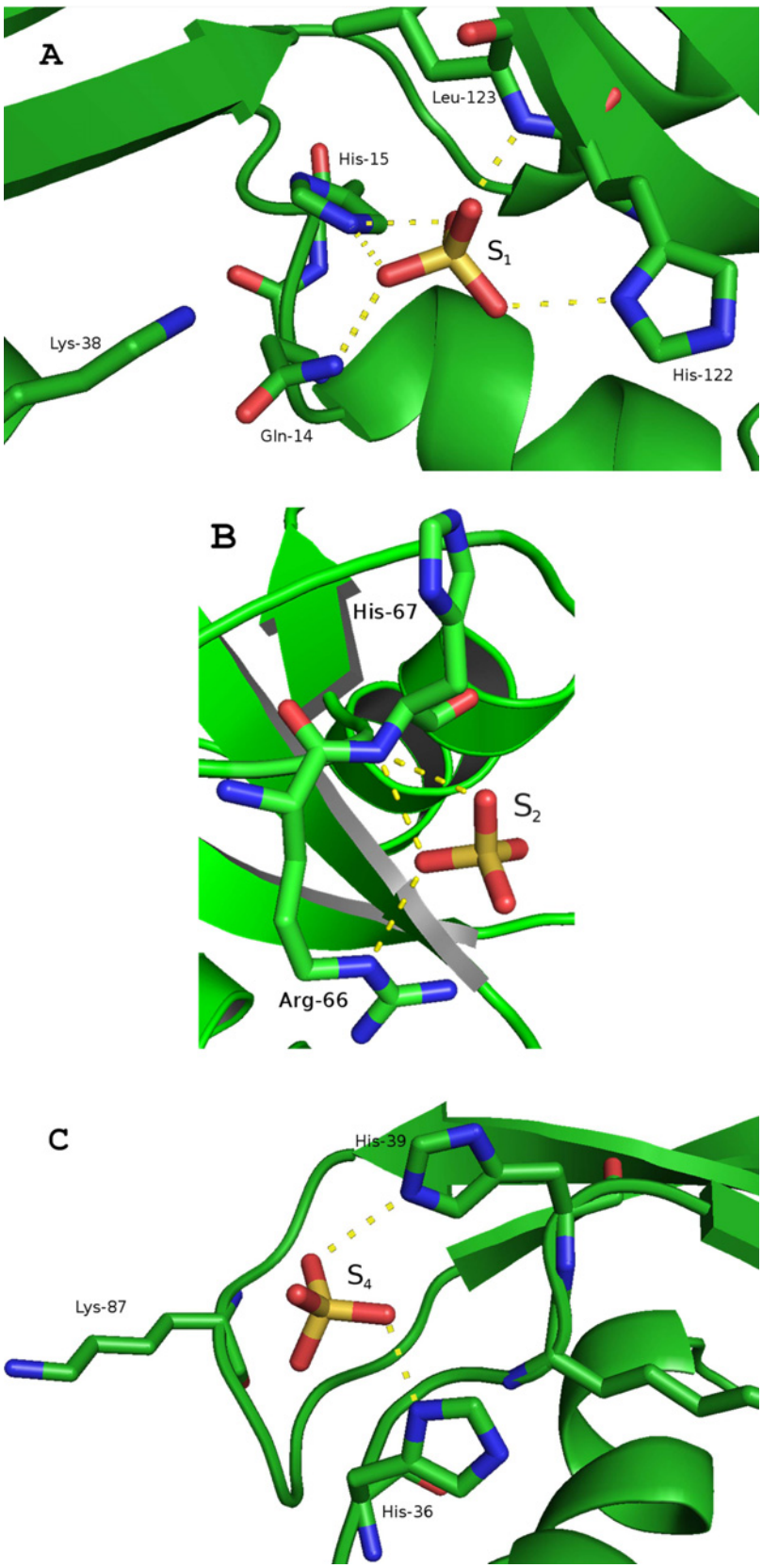

Figure 2 Detail of sulfate binding interactions in the RNase 6 crystal structure

Atoms involved in the protein–anion interactions are listed in Supplementary Table S3. The sulfate involved in the crystal packing (S3) is not shown. The structure was drawn with PyMol 1.7.2 (DeLano Scientific).

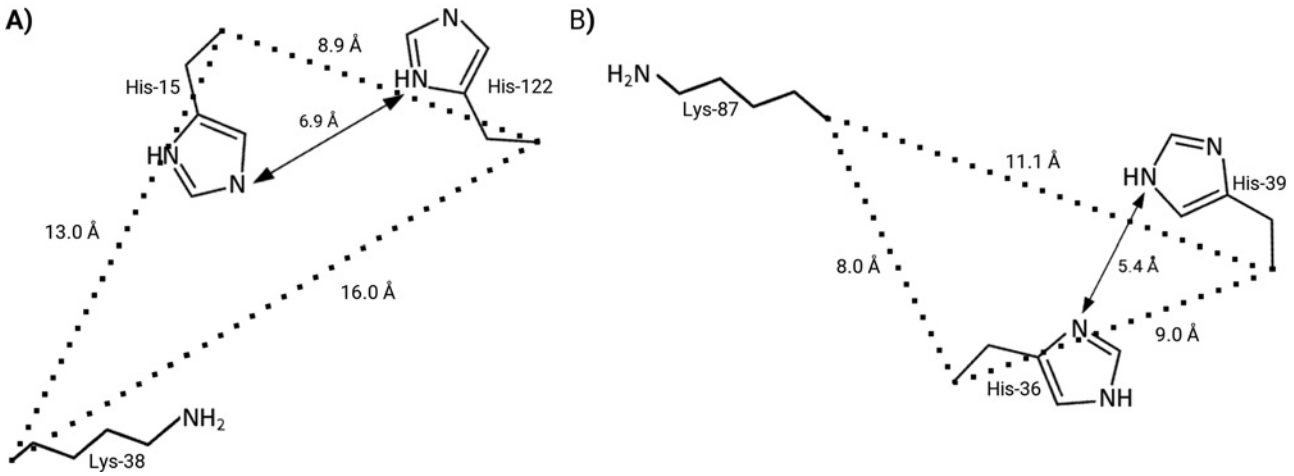

Figure 3 Illustrative scheme of RNase 6 main and putative secondary active sites

Illustrative scheme of the RNase 6 main active site (**A**) and the putative secondary site (**B**). CpA atom distances are labelled together with the hisitidine ND1 to NE2 respective distances. The figure was created with PyMol (DeLano Scientific).

Table 2 Kinetic parameters of RNases for dinucleotide and mononucleotide cyclic phosphate substrates

ND: not detected at the assayed conditions. *All assays were carried out in duplicate by a spectrophotometric assay as described in the Materials and methods section. Kinetic parameters were estimated from non-linear regression data using the GraFit program. †Values shown for RNase A activity are taken from [73–75].

		UpA	UpG	CpA	C>p
RNase 6	K_m (mM)*	2.63 ± 0.3	ND	1.22 ± 0.2	2.06 ± 0.3
	k_{cat} (s^{-1})	12.9 ± 1.1	ND	1.08 ± 0.1	$3.25 \times 10^{-3} \pm 0.06$
	k_{cat}/K_m ($s^{-1} \cdot M^{-1}$)	4.90×10^3	ND	8.85×10^2	1.60
RNase 3	K_m (mM)	2.7 ± 0.66	ND	1.7 ± 0.3	3 ± 0.53
	k_{cat} (s^{-1})	1.22 ± 0.12	ND	0.55 ± 0.06	$3.2 \times 10^{-3} \pm 5.1 \times 10^{-4}$
	k_{cat}/K_m ($s^{-1} \cdot M^{-1}$)	4.47×10^2	ND	3.23×10^2	1.07
RNase A†	K_m (mM)	0.7	2.0	0.5	1.06 ± 0.1
	k_{cat} (s^{-1})	2.69×10^3	1.38×10^2	2.3×10^3	2.28 ± 0.18
	k_{cat}/K_m ($s^{-1} \cdot M^{-1}$)	3.84×10^6	6.9×10^4	4.59×10^6	2.15×10^3

RNase 6 nucleotide-binding sites

The RNase 6 crystal structure was further analysed to elucidate the structural basis for the protein substrate specificity and kinetic properties. Comparison of the RNase 6 structure with RNase A indicated conservation of most residues at the B_1 site. In contrast, non-conserved substitutions were found for Phe[120] and Ser[123] RNase A counterpart residues. Phe[120] is observed in RNase A to contribute stacking interactions to fix the pyrimidine ring [37]. Nevertheless, a leucine residue in RNase 6, also present in RNase 3, might also contribute to shape the protein base binding hydrophobic cavity. In any case, the presence of Phe[120] in both RNase A and RNase 4, two very efficient RNase A family members, might also explain their relative higher catalytic activity. On the other hand, B_1 selectivity is considered to be dependent on a Thr–Asp dyad relative position. Thr[45]–Asp[83] interactions were attributed in RNase A to shift from cytidine to uridine preference [17]. However, in RNase 6, the presence of Gln[40], hydrogen-bonded to Asp[80] (Asp[83] counterpart), fixes the latter in a distinct orientation that might interfere in its interaction with Thr[42] (Thr[45] counterpart), and modifies the pyrimidine-binding mode. Additionally, RNase A and RNase 4 (an RNase with an unusually strong uridine preference [62]), have an hydrophobic residue at the Gln[40] position, which was considered to help locating the Thr[45] residue at the most favoured conformation for uridine base binding [63]. To note, Gln[40]–Asp[80] pair is unique to RNase 6 among the eight human canonical RNases (Figure 1). This scenario might explain in RNase 6 the observed increase K_m value for both UpA and CpA with respect to RNase A (Table 2). On the other hand, the orientation of Asp[80], closer to RNase A counterpart but clearly distinct from RNase 4, may explain RNase 6's moderate preference for uridine at the B_1 site (Table 3). Interestingly, the uridine predilection of RNase 4 would be mostly determined by Arg[101] that can directly interact with the uridine carbonyl group and bringes Asp[80] closer to the vicinity of Thr[45] [64]. Noteworthily, the presence of Arg[101] is characteristic of the RNase 4 lineage, whereas RNase A and RNase 6 have a lysine at this position which is pointing in the opposite direction.

Table 3 Catalytic activity ratio of RNases for the assayed nucleotides

ND: not detected at the assayed conditions. *Data for Poly(U):Poly(A) were taken from [76].

	CpA/UpA	CpA/C>p	Poly(C)/poly(U)	Poly(U)/poly(U):poly(A)
RNase 6	0.18	5.5×10^2	1.02	0.43
RNase 3	0.72	3.0×10^2	1.74	ND
RNase A*	1.20	2.1×10^3	8.14	307

Next, we analysed the RNase 6 structure at the secondary base site (B_2). Conservation of Asn^{68} and Asn^{64} (Asn^{71} and Asn^{67} in RNase A respectively) is observed. Notwithstanding, the presence of a non-conserved cationic residue at position 66 might alter significantly the region. Additionally, although there is a conservative substitution for Glu^{111} in RNase A (Asp^{107} in RNase 6), the distinct loop orientation, due to the presence of a proline residue in RNase 6, modifies considerably the region's putative interactions. Altogether, the B_2 site architecture would provide reduced binding interactions to the purine base, retaining a preference for adenine compared with guanine, as confirmed by our kinetic results (Tables 2 and 3, and Supplementary Table S4) and reported for most of the other tested mammalian RNase A family members [65–67]. Finally, we searched the RNase 6 structure for phosphate-binding sites that could contribute to the recognition of an RNA polymeric substrate, as described for RNase A [19]. Towards this aim, the protein nucleotide-binding mode was further analysed by molecular modelling.

Structure analysis by molecular modelling simulations

MD simulations were performed to predict the overall RNase 6 substrate-binding mode. Three independent runs were carried out for a total of 20 ns. All ligand positions were fully stabilized after a time lapse of 5 ns, showing a final average RMSD ranging from 0.15 to 0.3 nm. First of all, MD simulations were applied to RNase dinucleotide complexes taking as a model reference the RNase A–d(CpA) crystal structure [37]. Results indicated that the CpA and UpA dinucleotides could accommodate in a similar orientation into the RNase 6 catalytic cleft, showing no significant displacement from the original location (Figure 4). A close inspection of predicted RNase 6–dinucleotide interactions corroborated some of the structural features inferred from the crystal structure analysis. Equivalent interactions at the phosphate position suggested a conserved binding mode at the main phosphate-binding site (p_1). Noteworthily, although the starting position of His^{122} in the RNase 6 crystal was found in the inactive conformation, the residue was adjusted to its active orientation before modelling, remaining in the favoured orientation for catalysis after all MD simulations. Interestingly, together with equivalent relative positioning of Gln^{14}, His^{15} and His^{122}, the presence in the RNase 6 active-site neighbourhood of Lys^7 and Trp^{10} (Ala^4 and Lys^7 in RNase A) would account for significant differences at the p_1 environment.

The binding pattern described for RNase A was also mostly conserved for RNase 6 at the main pyrimidine base site (B_1). Leu^{123} in RNase 6 was observed to partially supply the Phe^{120}-stabilizing role in RNase A, but might induce a minor tilt of the ring plane. Interestingly, together with the conserved bidentate hydrogen bond between Thr^{42} and the pyrimidine base, the close-by Gln^{40} could directly interact with the Asp^{80} and the N3 atom of the pyrimidine base.

On the other hand, the comparison between the secondary base-binding site (B_2) of both RNases showed minor differences in the relative position of the adenine base, but a more pronounced base displacement for the guanine-containing dinucleotides. Equivalent hydrogen bond interactions to adenine were found in RNase 6 for Asn^{64} and Asn^{68} (Asn^{67} and Asn^{71} in RNase A), together with base-stacking interactions with His^{122} (His^{119} in RNase A). However, although the main determinants for adenine binding were conserved, we observed how the presence of Arg^{66}, unique to RNase 6, is significantly altering the environment. Indeed, in all of our predicted protein–dinucleotide complexes, we observed a salt bridge between Arg^{66} and Asp^{107}, which shifted the aspartate position from the corresponding RNase A anionic residue (Glu^{111}).

In particular, a major displacement from the original position was observed for the UpG dinucleotide in complex with both RNases. MD simulations indicated that the guanine base could not properly fit into the B_2 site, promoting non-canonical orientations, where the guanine base was partially displaced. Moreover, in both RNases, the bidentate hydrogen bond to Asn^{68} (Asn^{71} in RNase A) was partially lost. Variability among replicates in the dinucleotide positioning reminded the reported productive and non-productive binding mode for the crystallographic complexes of RNase A with 2′5′-UpG [68]. Additionally, interactions in both RNases between the guanine C2 amino group and the Asp^{107} (Glu^{111} in RNase A) residue would fix the base in a less favoured orientation, pushing away the phosphate from the main active site. Nonetheless, the relative UpG displacement from the original position was less pronounced in the predicted RNase A complex, probably due to the contribution of Phe^{120}-stacking interactions at B_1, that provide a better fixation of the pyrimidine base. On its side, the presence in RNase 6 of Lys^7 close to the active-site environment would favour the displacement of the phosphate towards the p_2 region.

Complementarily, to gain further insight into the protein nucleotide-binding mode we modelled an heptanucleotide complex taking the RNase A–d(ApTpApA) crystal structure [45] as a starting reference model (Figure 5). The oligonucleotide fitted nicely into the enzyme active cleft showing only significant differences from the RNase A-binding mode at the secondary substrate-binding sites. Figure 5 highlights the protein residues at hydrogen bond distance observed in the protein–heptanucleotide complex. Putative RNase 6 substrate-binding sites were ascribed for base and phosphate recognition (Supplementary Table S5). Together with conserved equivalent sites to RNase A, the predicted complex illustrated the presence in RNase 6 structure of unique interacting residues at the RNA 5′ end. A novel specific region at p_{-2} and p_{-3} sites would be conformed by His^{36}, His^{39} and Lys^{87}. In addition, stacking interactions between His^{36} and the base located at the B_{-2} position were also identified in the model.

Kinetic characterization of RNase 6

Next, we determined the RNase 6 enzymatic activity against a variety of RNA substrates to correlate the protein structure with its enzymatic properties. RNase 6 catalytic efficiency ratio was compared with RNase 3 and RNase A (Supplementary Table S4), as representative family members for low and high catalytic efficiency respectively [18,23,66].

First, kinetic parameters for RNase 6 were calculated for dinucleotide and cyclic mononucleotide substrates (Table 2). Comparison of K_m and k_{cat} values for cyclic mono- and di-nucleotides indicated that most of the decrease in the catalytic efficiency of RNase 6 in comparison with RNase A (from 100- to 1000-fold) is due to a reduction in the catalytic constant value. A side-by-side comparison of substrate relative ratio (Table 3) highlighted for RNase 6 a preference for uridine at the B_1 site and selectivity for adenine at B_2. Additionally, the enzyme activity was assayed against polymeric substrates (Table 3 and Supplementary Table S4). RNase 6 displayed a low catalytic efficiency for polynucleotides in comparison with RNase A (Supplementary Figure S2), showing a similar reduced relative catalytic activity as previously reported for RNase 3 [20]. Interestingly, we observed that RNase 6 had the ability to degrade the double stranded poly(U):poly(A) substrate, a property not shared by RNase 3.

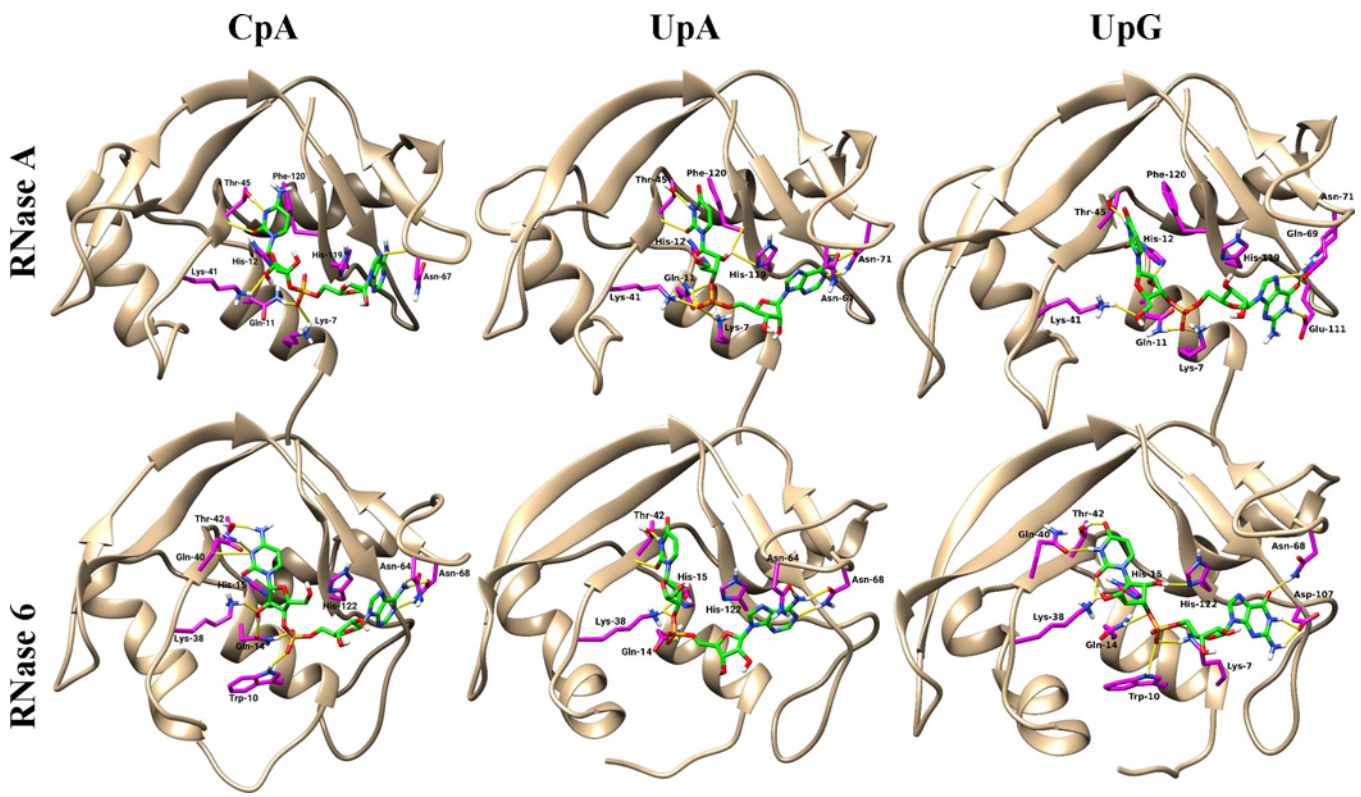

Figure 4 Predicted RNase 6 and RNase A structures in complex with dinucleotides

Predicted structure of RNase 6 and RNase A in complex with CpA, UpA and UpG dinucleotides after MD simulations, as detailed in the Materials and methods section. Nucleotides are coloured green. RNases interacting residues are coloured magenta. Hydrogen bonds are coloured yellow. Structures were drawn with UCSF Chimera 1.10 [77].

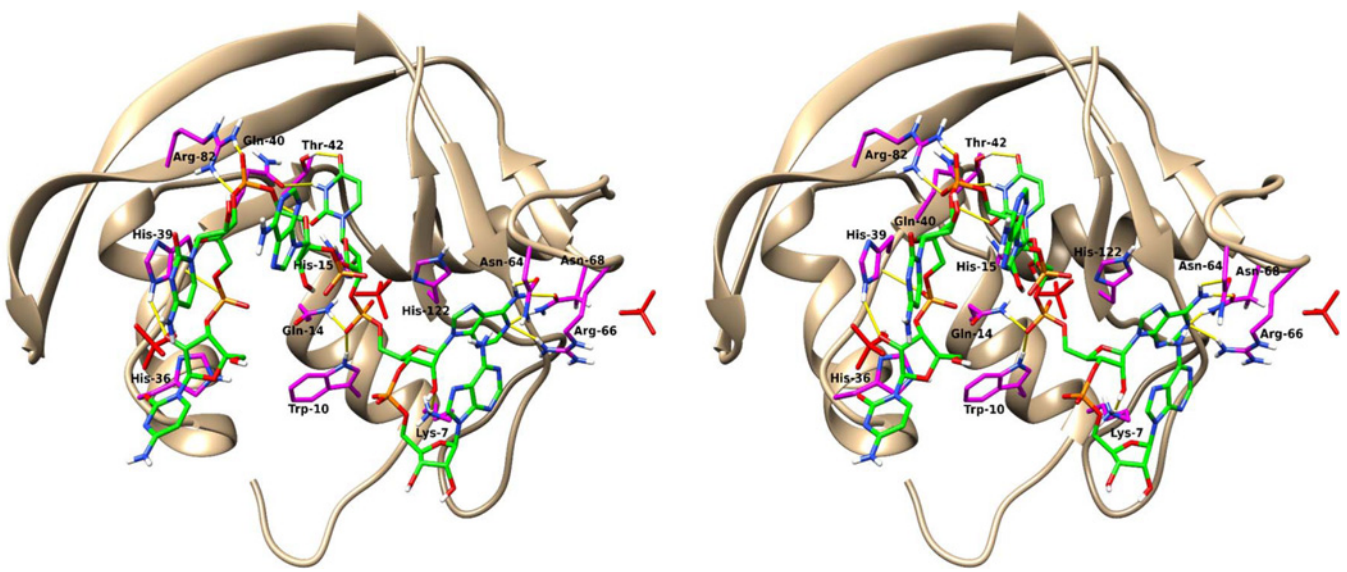

Figure 5 Stereo view of predicted RNase 6 heptanucleotide complex

RNase 6 in complex with CCCAUAA heptanucleotide after a MD simulation, as described in the Materials and methods section. The heptanucleotide is coloured green. Interacting residues of RNase 6 are coloured turquoise. Protein-interacting residues and ligand atoms are coloured according to their element. Hydrogen bonds are coloured yellow. Overlapped sulfate ions of the original coordinates of the crystal are coloured magenta. The structures were drawn with UCSF Chimera 1.10 [77].

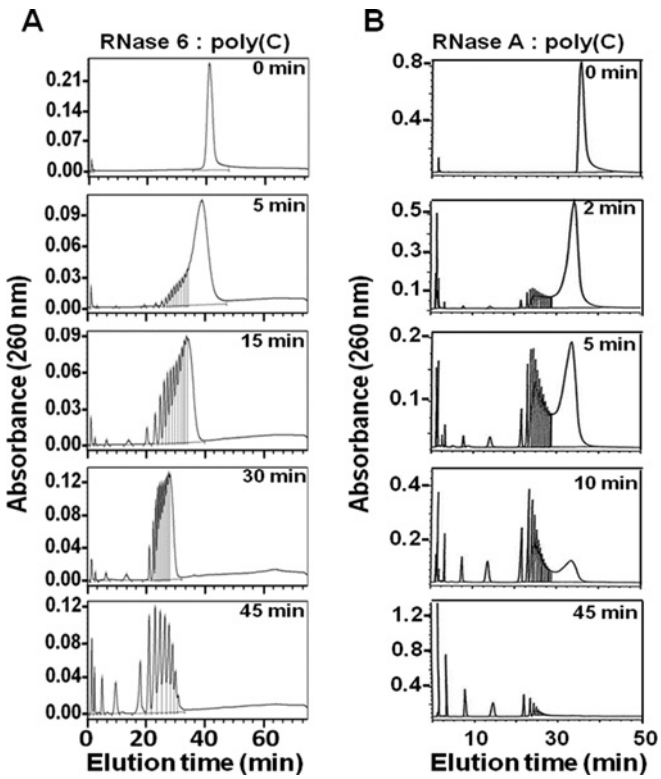

Figure 6 Analysis of polynucleotide cleavage pattern by RNase 6 and RNase A

Poly(C) cleavage pattern obtained by RNase 6 (**A**) compared with RNase A [27] (**B**). Chromatography profiles of poly(C) digestion products are shown at selected incubation times corresponding to representative steps of the catalysis process. See the Materials and methods section for substrate digestion conditions.

Complementarily, to evaluate the contribution of the RNase 6-specific subsite arrangement, we analysed the enzyme poly(C) cleavage pattern, as a model of polymeric substrate (Figure 6). The oligonucleotides obtained from the substrate digestion were eluted by reverse-phase chromatography, where the mononucleotide fraction is eluted at the initial conditions and oligonucleotides of increasing size are eluted at increasing retention times. The previously optimized methodology distinguishes between consecutive sizes up to eight or nine nucleotides, whereas the peaks corresponding to higher-molecular-mass components contain more than one oligonucleotide size due to the column discrimination power limitations [29]. Our previous work on RNase A cleavage pattern showed a decrease in the initial poly(C) peak followed by the formation of intermediate oligonucleotides with an average size of around six or seven residues, a pattern that supported the enzyme multisubsite structure providing a characteristic endonuclease-type activity [29]. Noteworthily, RNase 6 displayed a characteristic digestion profile differentiated from that previously obtained for RNase A [27], where there is first the formation of considerably large intermediates which are subsequently digested, giving rise to relatively shorter intermediates. Interestingly, the decrease in the original polynucleotide substrate was enhanced for RNase 6 at short incubation times. On the other hand, the predominance of smaller oligonucleotides did not take place until most of the high-molecular-mass polymeric substrate has been degraded, revealing a singularized cleavage pattern, that could be ascribed to a pronounced endonuclease mechanism.

Table 4 Relative catalytic activities for wild-type RNases 6 and 7 and mutant variants

ND: not detected at the assayed conditions. *Data expressed in percentage of activity in relation to the wild-type protein (%). Mean values were calculated from triplicate assays, showing in all cases a standard error below 10 %.

	UpA	CpA	Poly(U)	Poly(U):poly(A)
RNase 6	100	100	100	100
RNase 6-H15A*	13	14	77	63
RNase 6-H36R	94	86	36	40
RNase 6-H15A/H36A	ND	ND	15	5
RNase 7	100	100	100	100
RNase 7-H15A	ND	ND	3	7

Kinetic characterization of RNase 6 mutants

Analysis of the RNase 6 three-dimensional structure and molecular modelling predictions suggested that the enzyme facility to cleave polymeric substrates could be related to the presence of surface-exposed cationic residues that might facilitate the RNA anchorage and degradation. Noteworthily, the presence in RNase 6 of a histidine pair (His^{36}/His^{39}) (Figure 1 and Supplementary Figure S3) that adopts a configuration equivalent to the His^{15}/His^{122} dyad at the RNase main active site, suggested the existence of a secondary active centre (Figure 3). To evaluate this hypothesis, we designed mutant variants at His^{15} and His^{36}. First, the enzyme main active site was removed by His^{15} mutation to alanine. His^{15} in RNase 6 was selected as the RNase A His^{12} counterpart, where the corresponding H12A mutant was reported by Raines and co-workers to totally abolish the RNase A catalytic activity [69]. Additionally, His^{36} was mutated to arginine to remove the putative secondary catalytic histidine residue while retaining an exposed cationic charge. In addition, most RNase A family members, including RNase 7, the closest RNase 6 homologue, display an arginine residue at an equivalent position (Figure 1 and Supplementary Figure S3). Eventually, a double mutant (His15A/His36A) was engineered to evaluate simultaneously the removal of the main and secondary active sites.

Kinetic characterization of point mutants confirmed the key role of both His^{15} and His^{36} (Table 4). The contribution of His^{36} was found to be mostly critical for polymeric substrates. On the other hand, we observed how the RNase 6-H15A mutant was retaining a significantly high activity for polymeric substrates (approximately 35–40 % relative activity respect to wild-type RNase). Interestingly, for the assayed dinucleotides, a residual relative activity of approximately 15 % was observed, which was abolished by the double mutation. Moreover, the RNase 6-H15A activity was further compared with the corresponding RNase 7-H15A mutant (Table 4). The complete abolishment of activity for the RNase 7 active site mutant for dinucleotides, in contrast with RNase 6-H15A, corroborated the hypothesis. On the other hand, a remnant activity for polynucleotides is observed for both the RNase 6 double mutant and the RNase 7-H15A mutant. Likewise, residual catalytic activity for the RNase A-H12K/H119Q mutant was attributed to be solely promoted by the RNA structure distortion induced by the enzyme interaction [49].

Complementarily, the analysis of RNase 6 activity on polymeric substrates was also assayed on an activity staining gel and by the analysis of the polynucleotide digestion products. The side-by-side comparison of the polynucleotide cleavage product profiles obtained by incubation with both RNase 6-H15A and RNase 7-H15A mutants, devoid of the main active-site histidine residue, confirmed the presence in RNase 6 of another cleavage

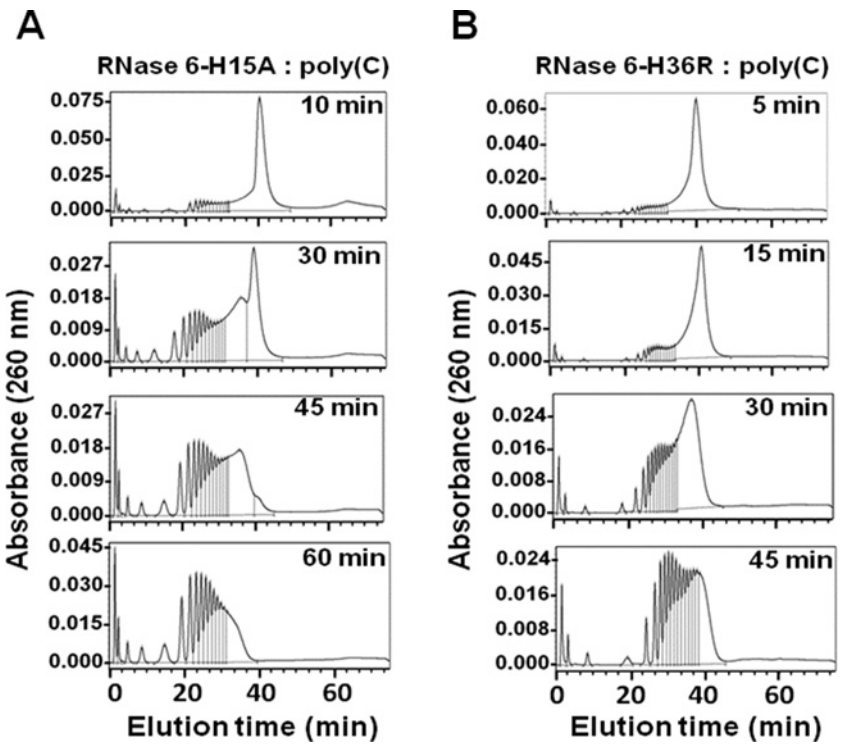

Figure 7 Analysis of polynucleotide cleavage pattern by RNase 6 mutants

Poly(C) cleavage pattern by RNase 6-H15A (**A**) and RNase 6-H36R (**B**) mutants. Chromatography profiles of poly(C) digestion products are shown at selected incubation times corresponding to representative steps of the catalysis process.

site. We observed that, using the same assay conditions, a considerable amount of activity is achieved with the RNase 6-H15A mutant, whereas non-significant activity is observed for the corresponding RNase 7-H15A mutant (Supplementary Figure S4). Comparison of both RNases activity on poly(C) together with RNase 6 mutants was also analysed by the zymogram technique (Supplementary Figure S2), where the RNase 6 double mutant displayed no detectable activity at even a 5-fold protein concentration. Interestingly, when comparing the poly(C) digestion pattern along with the His^{15} and 36 respective mutants' profiles we observe how both mutants shifted their product elution profile towards a more exonuclease-type pattern, accumulating shorter intermediates than the native enzyme at an earlier stage of the reaction. A similar profile progression was previously reported for RNase 3, described to present a subsites arrangement that would favour an exonuclease cleavage pattern [20].

DISCUSSION

We report in the present paper the first crystal structure RNase 6 in complex with sulfate anions (Table 1). The location of putative phosphate-binding sites was deduced from the position of the sulfate anions in the crystal structure (Figure 2 and Supplementary Table S3). Structural analysis and kinetic characterization were carried out to outline the protein nucleotide-binding sites arrangement. The first sulfate was ascribed to the main RNase phosphate-binding site, shared with the other RNase A family members [54,55,67]. Two additional sulfate anions were located at the protein-exposed cationic residues (His^{36}/His^{39} and Arg^{66}/His^{67}) and would correspond to secondary phosphate-binding sites. In particular, the His^{36}/His^{39} site is proposed as a novel and unique site within the RNase A family (Figures 1 and 3). Kinetic studies corroborated the involvement of His^{36} in enzyme catalysis (Table 4).

The contribution of RNase 6 novel secondary catalytic site in the catalytic mechanism was further analysed by the characterization of the enzyme polynucleotide cleavage pattern (Figure 6). The distribution of substrate digestion products indicated that the breakdown of the polymeric substrate was not a random process. The chromatography profiles revealed the preference of RNase 6 for the binding and cleavage of long RNA strands, where the broken phosphodiester bonds would be located considerably spaced apart from the end of the chain. By comparison with the previously characterized RNase A cleavage pattern [29], we concluded that the RNase 6 activity towards the polymeric substrate was even more endonucleolytic than the previously described for RNase A [19]. On the other hand, we observed how the poly(C) digestion profile underwent a pronounced shift in its cleavage pattern towards an exonuclease-type propensity when the main active-site histidine was mutated (Figure 7).

Complementarily, structural analysis also illustrated a well-defined substrate multisubsite arrangement for RNase 6. Interestingly, the predicted RNase 6 complex with a heptanucleotide by MD (Figure 5) revealed the presence of novel sites at the RNA 5′ end that would be ascribed to B_{-2} and p_{-2}/p_{-3} sites (Supplementary Table S5).

Interestingly, the RNase 6 structure revealed equivalent histidine ND1 to NE2 atomic distances for His^{15}/His^{122} and His^{36}/His^{39}, suggesting the presence of a secondary catalytic site. In addition, we observed stacking interactions between the B_{-2} base of the oligonucleotide and His^{39} in the predicted complex. However, structural analysis identified no additional residues for binding of adjacent bases at both phosphate

sides. Notwithstanding, kinetic data on dinucleotides indicated a reduced efficiency performance for this novel active site. Indeed, the percentage of remnant catalytic activity displayed by the RNase 6-H15A mutant is similar to the activity displayed by a previously engineered RNase A construct with an additional active site created at the p_2 phosphate-binding site position (RNase A-H7H10 variant) [49]. Likewise, a similar scenario might be envisaged for RNase 6 (see Supplementary Table S6 for comparison of estimated pK_a values for both RNase A His^7/His^{10} and RNase 6 His^{36}/His^{39} pairs). The calculated pK_a values for the corresponding histidine residues exposed at the protein surface indicated that neither of them underwent a significant decrease from the reference value that could provide an efficient base catalyst. Therefore, the predicted pK_a for His^{36} and His^{39} could not reproduce properly the efficient RNase A catalytic site [18,48]. And last, but not least, the presence of a third residue that could stabilize the transition state intermediate is not obvious. Interestingly, we find a neighbouring lysine residue (Lys^{87}) at the novel site environment that could meet the required RNase active site geometry (see Figure 3 for a schematic illustration). Unfortunately, the Lys^{87} side chain is disordered in the present RNase 6 crystal structure, providing no information on its proper orientation. However, the Lys^{87} side-chain conformation predicted by MD in the RNase 6–heptanucleotide complex did provide interactions with a phosphate located at the p_{-3} site (Supplementary Table S5). Noteworthily, Lys^{87} is found in all primate RNase 6 counterparts, but is absent from the murine sequence [9,15]. Interestingly, even if the RNase A mutant at Lys^{41} was shown to drastically reduce the enzyme catalytic efficiency [70], the insertion of a secondary catalytic site for RNase A at the p_2 location conformed by only a histidine dyad was also able to provide approximately 10–15 % of remnant activity in the absence of the main active site [49]. Likewise, the proposed novel RNase 6 secondary site would behave as a poor catalyst. In any case, the present kinetic data indicate that the presence of an anchoring site at the 36–39 region enhances significantly the enzyme catalysis of polymeric substrates. Interestingly, Sorrentino and co-workers' analysis of the enzymatic properties of RNase A family members suggested that the presence of a cationic cluster at that region, combined with an anionic residue at RNase A residue at the 83 position (Asp^{80} in RNase 6), correlated to the facility to destabilize dsRNA, exposing single-stranded stretches to the enzyme for cleavage [65,71,72]. Interestingly, RNase 6 shows a particular overabundance of histidine residues at its polypeptide sequence, in comparison with the other family homologues. As previously mentioned, most of these histidine residues are unique to the RNase 6 lineage (Figure 1B) [9,15]. In particular, we observed two cationic clusters (His^{36}/His^{39}) and (Arg^{66}/His^{67}) fully conserved among the more evolved primate members. To note, whereas His^{36} and His^{67} are found in all known primate primary structures, His^{39} and Arg^{66} are only present in the more evolved primates. Overall, evolutionary pressure would have drifted RNase 6 towards a slightly more cationic primary structure with an overabundance of histidine residues, providing a novel secondary active site. Future research should explore the ultimate implications in the protein's physiological function.

Conclusions

The RNase 6 first crystal structure has provided us the opportunity to explore its structure–function relationship. By combining structural analysis together with molecular modelling and kinetic characterization, we were able to spot key regions contributing to the enzyme's substrate specificity and catalytic properties. Results highlighted the RNase 6 multisubsite arrangement for substrate binding and the contribution of a secondary catalytic site that facilitates the cleavage of polynucleotide substrates. Further work is needed to fully characterize RNase 6's enzymatic properties towards the understanding of its specific mechanism of action.

AUTHOR CONTRIBUTION

Ester Boix and Mohammed Moussaoui conceived and designed the experimental work. Guillem Prats-Ejarque, Javier Arranz-Trullen, Jose Blanco, Mohammed Moussaoui and David Pulido performed the experiments. Guillem Prats-Ejarque, Mohammed Moussaoui, David Pulido, Victòria Nogués and Ester Boix analysed the data. Guillem Prats-Ejarque, Javier Arranz-Trullén and Ester Boix drafted the paper. Victòria Nogués, Mohammed Moussaoui, Guillem Prats-Ejarque and Ester Boix revised the final paper.

ACKNOWLEDGEMENTS

We thank all of the staff at the beamline BL13 (XALOC) at the ALBA Synchrotron Light Facility (Cerdanyola del Vallès, Spain) for their support during data collection. Heartfelt thanks go to Jordi Joanhuix and Fernando Gil for all of the help provided.

FUNDING

This work was supported by the Ministerio de Economía y Competitividad cofinanced by FEDER funds [grant numbers BFU2012-38695 and BES-2010-036238 (predoctoral fellowship to J.A.B.)]; the Generalitat de Catalunya [grant number 2014-SGR-728]; and the Universitat Autònoma de Barcelona [grant number 406-02-02/2013 (predoctoral fellowship to J.A.)].

REFERENCES

1 Boix, E. and Nogués, M.V. (2007) Mammalian antimicrobial proteins and peptides: overview on the RNase A superfamily members involved in innate host defence. Mol. Biosyst. **3**, 317–335 CrossRef PubMed
2 Rosenberg, H.F. (2008) RNase A ribonucleases and host defense: an evolving story. J. Leukoc. Biol. **83**, 1079–1087 CrossRef PubMed
3 Gupta, S.K., Haigh, B.J., Griffin, F.J. and Wheeler, T.T. (2012) The mammalian secreted RNases: mechanisms of action in host defence. Innate Immun. **19**, 86–97 CrossRef PubMed
4 Zhang, J. and Rosenberg, H.F. (2002) Complementary advantageous substitutions in the evolution of an antiviral RNase of higher primates. Proc. Natl. Acad. Sci. U.S.A. **99**, 5486–5491 CrossRef PubMed
5 Pizzo, E. and D'Alessio, G. (2007) The success of the RNase scaffold in the advance of biosciences and in evolution. Gene **406**, 8–12 CrossRef PubMed
6 Hamann, K.J., Ten, R.M., Loegering, D.A., Jenkins, R.B., Heise, M.T., Schad, C.R., Pease, L.R., Gleich, G.J. and Barker, R.L. (1990) Structure and chromosome localization of the human eosinophil-derived neurotoxin and eosinophil cationic protein genes: evidence for intronless coding sequences in the ribonuclease gene superfamily. Genomics **7**, 535–546 CrossRef PubMed
7 Zhang, J., Dyer, K.D. and Rosenberg, H.F. (2002) RNase 8, a novel RNase A superfamily ribonuclease expressed uniquely in placenta. Nucleic Acids Res. **30**, 1169–1175 CrossRef PubMed
8 Rosenberg, H.F. and Dyer, K.D. (1996) Molecular cloning and characterization of a novel human ribonuclease (RNase k6): increasing diversity in the enlarging ribonuclease gene family. Nucleic Acids Res. **24**, 3507–3513 CrossRef PubMed
9 Deming, M.S., Dyer, K.D., Bankier, A.T., Piper, M.B., Dear, P.H. and Rosenberg, H.F. (1998) Ribonuclease k6: chromosomal mapping and divergent rates of evolution within the RNase A gene superfamily. Genome Res. **8**, 599–607 PubMed
10 Becknell, B., Eichler, T.E., Beceiro, S., Li, B., Easterling, R.S., Carpenter, A.R., James, C.L., McHugh, K.M., Hains, D.S., Partida-Sanchez, S. and Spencer, J.D. (2015) Ribonucleases 6 and 7 have antimicrobial function in the human and murine urinary tract. Kidney Int. **87**, 151–161 CrossRef PubMed
11 Spencer, J.D., Schwaderer, A.L., Wang, H., Bartz, J., Kline, J., Eichler, T., DeSouza, K.R., Sims-Lucas, S., Baker, P. and Hains, D.S. (2013) Ribonuclease 7, an antimicrobial peptide upregulated during infection, contributes to microbial defense of the human urinary tract. Kidney Int. **83**, 615–625 CrossRef PubMed

12 Jelicic, K., Cimbro, R., Nawaz, F., Huang, D.W., Zheng, X., Yang, J., Lempicki, R.A., Pascuccio, M., Van Ryk, D., Schwing, C. et al. (2013) The HIV-1 envelope protein gp120 impairs B cell proliferation by inducing TGF-beta1 production and FcRL4 expression. Nat. Immunol. **14**, 1256–1265 CrossRef PubMed

13 Zhang, J., Dyer, K.D. and Rosenberg, H.F. (2000) Evolution of the rodent eosinophil-associated RNase gene family by rapid gene sorting and positive selection. Proc. Natl. Acad. Sci. U.S.A. **97**, 4701–4706 CrossRef PubMed

14 McDevitt, A.L., Deming, M.S., Rosenberg, H.F. and Dyer, K.D. (2001) Gene structure and enzymatic activity of mouse eosinophil-associated ribonuclease 2. Gene **267**, 23–30 CrossRef PubMed

15 Dyer, K.D., Rosenberg, H.F. and Zhang, J. (2004) Isolation, characterization, and evolutionary divergence of mouse RNase 6: evidence for unusual evolution in rodents. J. Mol. Evol. **59**, 657–665 CrossRef PubMed

16 Richards, F.M. and Wyckoff, H.W. (1971) Bovine pancreatic ribonuclease. Enzymes IV 647–806 CrossRef

17 Raines, R.T. (1998) Ribonuclease A. Chem. Rev. **98**, 1045–1065 CrossRef PubMed

18 Cuchillo, C.M., Nogués, M.V. and Raines, R.T. (2011) Bovine pancreatic ribonuclease: fifty years of the first enzymatic reaction mechanism. Biochemistry **50**, 7835–7841 CrossRef PubMed

19 Nogués, M.V., Moussaoui, M., Boix, E., Vilanova, M., Ribó, M. and Cuchillo, C.M. (1998) The contribution of noncatalytic phosphate-binding subsites to the mechanism of bovine pancreatic ribonuclease A. Cell. Mol. Life Sci. **54**, 766–774 CrossRef PubMed

20 Boix, E., Nikolovski, Z., Moiseyev, G., Rosenberg, H.F., Cuchillo, C.M. and Nogues, M.V. (1999) Kinetic and product distribution analysis of human eosinophil cationic protein indicates a subsite arrangement that favors exonuclease-type activity. J. Biol. Chem. **274**, 15605–15614 CrossRef PubMed

21 Rosenberg, H.F. (1995) Recombinant human eosinophil cationic protein. Ribonuclease activity is not essential for cytotoxicity. J. Biol. Chem. **270**, 7876–7881 CrossRef PubMed

22 Harder, J. and Schroder, J.-M. (2002) RNase 7, a novel innate immune defense antimicrobial protein of healthy human skin. J. Biol. Chem. **277**, 46779–46784 CrossRef PubMed

23 Boix, E., Salazar, V.A., Torrent, M., Pulido, D., Nogués, M.V. and Moussaoui, M. (2012) Structural determinants of the eosinophil cationic protein antimicrobial activity. Biol. Chem. **393**, 801–815 CrossRef PubMed

24 Torrent, M., Sanchez, D., Buzon, V., Nogues, M.V, Cladera, J. and Boix, E. (2009) Comparison of the membrane interaction mechanism of two antimicrobial RNases: RNase 3/ECP and RNase 7. Biochim. Biophys. Acta **1788**, 1116–1125 CrossRef PubMed

25 Libonati, M. and Sorrentino, S. (2001) Degradation of double-stranded RNA by mammalian pancreatic-type ribonucleases. Methods Enzymol. **341**, 234–248 CrossRef PubMed

26 Bravo, J., Fernández, E., Ribó, M., Dellorens, R. and Cuchillo, C.M. (1994) A versatile negative-staining ribonuclease zymogram. Anal. Biochem. **219**, 82–86 CrossRef PubMed

27 Moussaoui, M., Guasch, A., Boix, E., Cuchillo, C.M. and Nogués, M.V. (1996) The role of non-catalytic binding subsites in the endonuclease activity of bovine pancreatic ribonuclease A. J. Biol. Chem. **271**, 4687–4692 CrossRef PubMed

28 Nogues, M.V. and Cuchillo, C.M. (2001) Analysis by HPLC of distributive activities and the synthetic (back) reaction of pancreatic-type ribonucleases. Methods Mol. Biol. **160**, 15–24 PubMed

29 Cuchillo, C.M., Moussaoui, M., Barman, T., Travers, F. and Nogues, M.V. (2002) The exo- or endonucleolytic preference of bovine pancreatic ribonuclease A depends on its subsites structure and on the substrate size. Protein Sci. **11**, 117–128 CrossRef PubMed

30 Kabsch, W. (2010) XDS. Acta Crystallogr. D Biol. Crystallogr. **66**, 125–132 CrossRef PubMed

31 Huang, Y.C., Lin, Y.M., Chang, T.W., Wu, S.H., Lee, Y.S., Chang, M.D., Chen, C., Wu, S.J. and Liao, Y.D. (2007) The flexible and clustered lysine residues of human ribonuclease 7 are critical for membrane permeability and antimicrobial activity. J. Biol. Chem. **282**, 4626–4633 CrossRef PubMed

32 Adams, P.D., Afonine, P.V, Bunkoczi, G., Chen, V.B., Davis, I.W., Echols, N., Headd, J.J., Hung, L.-W., Kapral, G.J., Grosse-Kunstleve, R.W. et al. (2010) PHENIX: a comprehensive Python-based system for macromolecular structure solution. Acta Crystallogr. D Biol. Crystallogr. **66**, 213–221 CrossRef PubMed

33 Emsley, P. and Cowtan, K. (2004) Coot: model-building tools for molecular graphics. Acta Crystallogr. D Biol. Crystallogr. **60**, 2126–2132 CrossRef PubMed

34 Vaguine, A.A., Richelle, J. and Wodak, S.J. (1999) SFCHECK: a unified set of procedures for evaluating the quality of macromolecular structure-factor data and their agreement with the atomic model. Acta Crystallogr. D Biol. Crystallogr. **55**, 191–205 CrossRef PubMed

35 Hooft, R.W., Vriend, G., Sander, C. and Abola, E.E. (1996) Errors in protein structures. Nature **23**, 381

36 Pronk, S., Páll, S., Schulz, R., Larsson, P., Bjelkmar, P., Apostolov, R., Shirts, M.R., Smith, J.C., Kasson, P.M., Van Der Spoel, D. et al. (2013) GROMACS 4.5: a high-throughput and highly parallel open source molecular simulation toolkit. Bioinformatics **29**, 845–854 CrossRef PubMed

37 Zegers, I., Maes, D., Poortmans, F., Palmer, R. and Wyns, L. (1994) The structures of RNase A complexed with 3′ -CMP and d(CpA): active site conformation and conserved water molecules. Protein Sci. **3**, 2322–2339 CrossRef PubMed

38 Lindorff-Larsen, K., Piana, S., Palmo, K., Maragakis, P., Klepeis, J.L., Dror, R.O. and Shaw, D.E. (2010) Improved side-chain torsion potentials for the Amber ff99SB protein force field. Proteins **78**, 1950–1958 PubMed

39 Jorgensen, W.L., Chandrasekhar, J., Madura, J.D., Impey, R.W. and Klein, M.L. (1983) Comparison of simple potential functions for simulating liquid water. J. Chem. Phys. **79**, 926 CrossRef

40 Darden, T., York, D. and Pedersen, L. (1993) Particle mesh Ewald: an N·log(N) method for Ewald sums in large systems. J. Chem. Phys. **98**, 10089 CrossRef

41 Essmann, U., Perera, L., Berkowitz, M.L., Darden, T., Lee, H. and Pedersen, L.G. (1995) A smooth particle mesh Ewald method. J. Chem. Phys. **103**, 8577 CrossRef

42 Hess, B. (2008) P-LINCS: a parallel linear constraint solver for molecular simulation. J. Chem. Theory Comput. **4**, 116–122 CrossRef PubMed

43 Parrinello, M. and Rahman, A. (1981) Polymorphic transitions in single crystals: a new molecular dynamics method. J. Appl. Phys. **52**, 7182–7190 CrossRef

44 Nosé, S. and Klein, M.L. (1983) Constant pressure molecular dynamics for molecular systems. Mol. Phys. **50**, 1055–1076 CrossRef

45 Fontecilla-Camps, J.C., de Llorens, R., le Du, M.H. and Cuchillo, C.M. (1994) Crystal structure of ribonuclease A.d(ApTpApApG) complex. Direct evidence for extended substrate recognition. J. Biol. Chem. **269**, 21526–21531 PubMed

46 Morris, G.M., Huey, R., Lindstrom, W., Sanner, M.F., Belew, R.K., Goodsell, D.S. and Olson, A.J. (2009) AutoDock4 and AutoDockTools4: automated docking with selective receptor flexibility. J. Comput. Chem. **30**, 2785–2791 CrossRef PubMed

47 Kilambi, K.P. and Gray, J.J. (2012) Rapid calculation of protein pKa values using Rosetta. Biophys. J. **103**, 587–595 CrossRef PubMed

48 Fisher, B.M., Schultz, L.W. and Raines, R.T. (1998) Coulombic effects of remote subsites on the active site of ribonuclease A. Biochemistry **37**, 17386–17401 CrossRef PubMed

49 Moussaoui, M., Cuchillo, C.M. and Nogués, M.V. (2007) A phosphate-binding subsite in bovine pancreatic ribonuclease A can be converted into a very efficient catalytic site. Protein Sci **16**, 99–109 CrossRef PubMed

50 Krissinel, E. and Henrick, K. (2007) Inference of macromolecular assemblies from crystalline state. J. Mol. Biol. **372**, 774–797 CrossRef PubMed

51 Rico, M., Gallego, E., Santoro, J., Bermejo, F.J., Nieto, J.L. and Herranz, J. (1984) On the fundamental role of the Glu 2- ... Arg 10 + salt bridge in the folding of isolated ribonuclease A S-peptide. Biochem. Biophys. Res. Commun. **123**, 757–763 CrossRef PubMed

52 Chatani, E. and Hayashi, R. (2001) Functional and structural roles of constituent amino acid residues of bovine pancreatic ribonuclease A. J. Biosci. Bioeng. **92**, 98–107 CrossRef PubMed

53 Berisio, R., Sica, F., Lamzin, V.S., Wilson, K.S., Zagari, A. and Mazzarella, L. (2002) Atomic resolution structures of ribonuclease A at six pH values. Acta Crystallogr. D Biol. Crystallogr. **58**, 441–450 CrossRef PubMed

54 Fedorov, A.A., Joseph-McCarthy, D., Fedorov, E., Sirakova, D., Graf, I. and Almo, S.C. (1996) Ionic interactions in crystalline bovine pancreatic ribonuclease A. Biochemistry **35**, 15962–15979 CrossRef PubMed

55 Leonidas, D.D., Boix, E., Prill, R., Suzuki, M., Turton, R., Minson, K., Swaminathan, G.J., Youle, R.J. and Acharya, K.R. (2001) Mapping the ribonucleolytic active site of eosinophil-derived neurotoxin (EDN): high resolution crystal structures of EDN complexes with adenylic nucleotide inhibitors. J. Biol. Chem. **276**, 15009–15017 CrossRef PubMed

56 Boix, E., Pulido, D., Moussaoui, M., Nogues, M.V. and Russi, S. (2012) The sulfate-binding site structure of the human eosinophil cationic protein as revealed by a new crystal form. J. Struct. Biol. **179**, 1–9 CrossRef PubMed

57 Holloway, D.E., Chavali, G.B., Hares, M.C., Subramanian, V. and Acharya, K.R. (2005) Structure of murine angiogenin: features of the substrate- and cell-binding regions and prospects for inhibitor-binding studies. Acta Crystallogr. D Biol. Crystallogr. **61**, 1568–1578 CrossRef PubMed

58 Borkakoti, N. (1983) The active site of ribonuclease A from the crystallographic studies of ribonuclease-A-inhibitor complexes. Eur. J. Biochem. **132**, 89–94 CrossRef PubMed

59 Berisio, R., Lamzin, V.S., Sica, F., Wilson, K.S., Zagari, A. and Mazzarella, L. (1999) Protein titration in the crystal state. J. Mol. Biol. **292**, 845–854 CrossRef PubMed

60 deMel, V.S., Martin, P.D., Doscher, M.S. and Edwards, B.F. (1992) Structural changes that accompany the reduced catalytic efficiency of two semisynthetic ribonuclease analogs. J. Biol. Chem. **267**, 247–256 PubMed

61 Schultz, L.W., Quirk, D.J. and Raines, R.T. (1998) His...Asp catalytic dyad of ribonuclease A: structure and function of the wild-type, D121N, and D121A enzymes. Biochemistry **37**, 8886–8898 CrossRef PubMed

62 Hofsteenge, J., Vicentini, A. and Zelenko, O. (1998) Ribonuclease 4, an evolutionarily highly conserved member of the superfamily. Cell. Mol. Life Sci. **54**, 804–810 CrossRef PubMed

63 Vicentini, A.M., Kote-Jarai, Z. and Hofsteenge, J. (1996) Structural determinants of the uridine-preferring specificity of RNase PL3. Biochemistry **35**, 9128–9132 CrossRef PubMed
64 Terzyan, S.S., Peracaula, R., de Llorens, R., Tsushima, Y., Yamada, H., Seno, M., Gomis-Ruth, F.X. and Coll, M. (1999) The three-dimensional structure of human RNase 4, unliganded and complexed with d(Up), reveals the basis for its uridine selectivity. J. Mol. Biol. **285**, 205–214 CrossRef PubMed
65 Sorrentino, S. (1998) Human extracellular ribonucleases: multiplicity, molecular diversity and catalytic properties of the major RNase types. Cell. Mol. Life Sci. **54**, 785–794 CrossRef PubMed
66 Sorrentino, S. (2010) The eight human "canonical" ribonucleases: molecular diversity, catalytic properties, and special biological actions of the enzyme proteins. FEBS Lett. **584**, 2194–2200 CrossRef PubMed
67 Boix, E., Blanco, J.A., Nogués, M.V. and Moussaoui, M. (2013) Nucleotide binding architecture for secreted cytotoxic endoribonucleases. Biochimie **95**, 1087–1097 CrossRef PubMed
68 Vitagliano, L., Merlino, A., Zagari, A. and Mazzarella, L. (2000) Productive and nonproductive binding to ribonuclease A: X-ray structure of two complexes with uridylyl(2',5')guanosine. Protein Sci. **9**, 1217–1225 CrossRef PubMed
69 Park, C., Schultz, L.W. and Raines, R.T. (2001) Contribution of the active site histidine residues of ribonuclease A to nucleic acid binding. Biochemistry **40**, 4949–4956 CrossRef PubMed
70 Trautwein, K., Holliger, P., Stackhouse, J. and Benner, S.A. (1991) Site-directed mutagenesis of bovine pancreatic ribonuclease: lysine-41 and aspartate-121. FEBS Lett. **281**, 275–277 CrossRef PubMed
71 Libonati, M. and Sorrentino, S. (1992) Revisiting the action of bovine ribonuclease A and pancreatic-type ribonucleases on double-stranded RNA. Mol. Cell. Biochem. **117**, 139–151 CrossRef PubMed
72 Yakovlev, G., Moiseyev, G.P., Sorrentino, S., De Prisco, R. and Libonati, M. (1997) Single-strand-preferring RNases degrade double-stranded RNAs by destabilizing its secondary structure. J. Biomol. Struct. Dyn. **15**, 243–250 CrossRef PubMed
73 Shapiro, R., Fett, J.W., Strydom, D.J. and Vallee, B.L. (1986) Isolation and characterization of a human colon carcinoma-secreted enzyme with pancreatic ribonuclease-like activity. Biochemistry **25**, 7255–7264 CrossRef PubMed
74 Follmann, H., Wieker, H.J. and Witzel, H. (1967) On the mechanism of the ribonuclease reaction. 2. The pre-ordering in the substrate as the accelerating factor in cinucleoside phosphates and analagous compounds. Eur. J. Biochem. **1**, 243–250 CrossRef PubMed
75 Boix, E., Nogues, M.V., Schein, C.H., Benner, S.A. and Cuchillo, C.M. (1994) Reverse transphosphorylation by ribonuclease A needs an intact p2-binding site. J. Biol. Chem. **269**, 2529–2534 PubMed
76 Sorrentino, S. and Glitz, D.G. (1991) Ribonuclease activity and substrate preference of human eosinophil cationic protein (ECP). FEBS Lett. **288**, 23–26 CrossRef PubMed
77 Pettersen, E.F., Goddard, T.D., Huang, C.C., Couch, G.S., Greenblatt, D.M., Meng, E.C. and Ferrin, T.E. (2004) UCSF Chimera – a visualization system for exploratory research and analysis. J. Comput. Chem. **25**, 1605–1612 CrossRef PubMed

Received 4 January 2016/23 March 2016; accepted 24 March 2016
Accepted Manuscript online 24 March 2016, doi:10.1042/BCJ20160245